Int. J. Electrochem. Sci., 17 **(2022)** Article Number: 220639, doi: 10.20964/2022.06.38

International Journal of
ELECTROCHEMICAL
SCIENCE
www.electrochemsci.org

A Palladium and Nickel Composite Catalyst Composed of Huge Spherical Particles and Sawdust-Shaped Particles Showing Significant Electrocatalytic Activities towards Ethanol Oxidation Reaction (EOR)

Keqiang Ding[1,2,*], *Boxia Li*[1], *Fujuan Shi*[1], *Mengyao Di*[1], *Mengying Yan*[1], *Lin Xu*[1], *Xueying Wang*[1], *Hui Wang*[2]

[1] Hebei Key Laboratory of Inorganic Nano-materials, Hebei Key Laboratory of Organic Functional Molecules, College of Chemistry and Materials Science, Hebei Normal University, Shijiazhuang, 050024, China
[2] Hebei LingDian New Energy Technology Co., Ltd, Tangshan, 064200, China
[*]E-mail: dkeqiang@263.net

Received: 1 March 2022 / *Accepted:* 31 March 2022 / *Published:* 7 May 2022

In this work, a palladium (Pd) and nickel (Ni) (denoted as Pd-Ni) composite catalyst composed of huge spherical particles and sawdust-shaped particles for EOR was prepared through a two-step approach in which Ni_2O_3 and glucose and $PdO{\cdot}H_2O$ were employed as the reactants. Firstly, a precursor containing NiO and carbon material (abbreviated as NiO/C) was prepared via a hydrothermal process assisted air calcination method using Ni_2O_3 and glucose as the starting materials. And in this step, four different amounts of Ni_2O_3 (0 g, 0.05 g, 0.10 g and 0.15 g) were added in the starting preparation system, respectively, generating four types of NiO/C precursors (denoted as p_0, p_1, p_2 and p_3). Secondly, above one kind of NiO/C precursor reacted with PdO hydrothermally in an autoclave under certain conditions to prepare the final catalysts. That is, the final catalysts prepared in the presence of p_0, p_1, p_2 and p_3 were respectively called as catalyst c_0, c_1, c_2 and c_3. As revealed by the SEM images, besides several huge spherical particles, some irregular small particles and sawdust-shaped particles were respectively exhibited in c_0 and c_1. While in the case of c_2 and c_3, only some agglomerates assembled by powder-shaped particles were displayed clearly. On the basis of XRD and XPS measurement results, except for the carbon materials, metallic Pd and PdO were indicated to be the main substances of c_0, NiO and metallic Pd were demonstrated to be the major chemical compounds of c_1, c_2 and c_3. Most importantly, as indicated by CV and CA tests, c_1, c_2 and c_3 showed significantly improved electrocatalytic activities towards EOR as compared to the case of using c_0, exhibiting a decreasing order, namely, $c_1 > c_3 > c_2 > c_0$. In the CV test, the forward peak current density (32.4 mA cm^{-2}) for EOR on c_1 at 50 mV s^{-1} was about 36 times higher than that measured on c_0 (0.9 mA cm^{-2}). As indicated by the CA test, the polarized current densities of EOR measured under -0.3 V at 600 s were recorded to be 0.2, 14.7, 3.9 and 7.7 mA cm^{-2} for the case of using c_0, c_1, c_2 and c_3, respectively. Especially, even after 7200 s, the polarized current density of EOR on c_1 was still maintained to be as high as 2.68 mA cm^{-2}, showing an excellent durability. Showing the synthesis of a novel precursor of NiO/C and preparing a new high

performance Pd-Ni composite catalyst for EOR were the main contributions of this work, which was very helpful to the further development of Pd-Ni based EOR electrocatalysts.

Keywords: precursor; Ni_2O_3; Pd-Ni composite catalyst; hydrothermal process assisted air calcination method; ethanol oxidation reaction

1. INTRODUCTION

It is widely accepted that the massive emission of carbon dioxide (CO_2) is one of the main reasons causing global warming [1, 2]. Generally, CO_2 emitted in the atmosphere is regarded to be mainly resulted from industrial production and transportation [3]. Therefore, green industry and low carbon transportation are urgently announced to be a national strategy by many nations so as to greatly reduce the emission of CO_2 mitigating the global warming [4, 5]. As a result, how to extremely reduce the emission of CO_2 has become a subject that all mankind must face [6]. In terms of low carbon transportation, replacing oil-fired motor vehicles using electric vehicle (EV) is extensively believed to be a feasible way to remarkably reduce the massive emission of CO_2 [7]. Consequently, battery as the core part of an EV has been paid unprecedented research attention especially in recent years [8].

As compared to other kinds of batteries, fuel cells, mainly due to their higher energy densities and environment friendliness, are thought as one of the most promising kinds of battery to power an EV [9]. Among all existing fuel cells, direct ethanol fuel cells (DEFCs) [10] are selected as one kind of suitable fuel cell to drive an EV because DEFCs, as compared to the direct methanol fuel cells (DMFCs) [11], have a higher energy density and a satisfied environmental issue (ethanol is non-toxic). As is known to all, in the anodic part of a DEFC, electrons are released by the ethanol oxidation reaction (EOR), and then, the released electrons are transferred from the external circuit to the cathodic part of a DEFC to the react with O_2 achieving an electronic circuit [12]. Hence, electrocatalysts used for EOR, as the key part of the EOR process, played a major role in affecting the final battery performance of a DEFC.

Of late, besides platinum (Pt) based electrocatalysts [13], palladium (Pd) based electrocatalysts were also found to be able to electrochemically catalyze the EOR especially in an alkaline medium [14]. Consequently, Pd-based electrocatalysts, mainly owing to the abundant reserves of Pd as compared to that of Pt [15], have received widespread attention recently since the cost effectiveness of a catalysts was very crucial to its final commercialization in the DEFCs based EV. In the last several years, many kinds of Pd based binary catalysts, such as Pd-Sn [16], Pd-Ag [17] and etc. [18], have been urgently developed with an intention to further reduce the preparation cost of a Pd-based catalyst while maintaining its satisfied electrocatalytic activity towards EOR. As one typical Pd-based binary catalyst for EOR, Pd-Ni composite electrocatalyst [19], mainly due to the non-toxicity of Ni as well as its excellent electrocatalytic activity for EOR, was considered to be the most likely electrocatalyst to replace the pure Pd electrocatalyst in the near future.

Till present, many kinds of Ni containing chemicals have been employed as the Ni source to prepare Pd-Ni composite catalysts. For example, Yi's research team [20] reported that binary Pd-Ni

nanocatalysts with low Pd loading could be facilely prepared through a two chemical reduction process in which $NiCl_2$ and $PdCl_2$ were employed as the beginning materials. A Pd-Ni nanocatalyst was also prepared by Gojković and his collaborators [21] using a conventional redox method in which $Ni(HCOO)_2$ and $PdCl_2$ were used as the starting materials and $NaBH_4$ as the reducing agent. In 2019, MnO_2/Vulcan supported Pd-Ni nanoparticles were skillfully prepared by Ghaedi's group [22] via a chemical reduction in which $PdCl_2$ and $Ni(NO_3)_2$ were utilized as the starting materials and $NaBH_4$ also as the reducing agent. Zhang and his co-workers [23] successfully prepared palladium-based crystalline@amorphous core-shell nanoplates through a facile wet chemical method in which $PdCl_2$ and $NiCl_2{\cdot}6H_2O$ were used as the starting chemicals. In 2021, Wang's team [24] prepared PdNi/Ni nanotubes via a traditional chemical reaction where $NiCl_2$ and Na_2PdCl_4 were respectively employed as the Ni and Pd sources. Except for above conventional redox reactions, very recently, an electrochemical method was also introduced to prepare Pd-Ni composite catalyst. For instance, a bimetallic PdNi nanocoating was successfully prepared by Cornell's group [25] through an electrodeposition technique in which the electrodeposition solution mainly contained $Ni(NO_3)_2$ and $PdCl_2$. Although many Ni-containing chemicals have been employed as the nickel source to prepare Pd-Ni composites, to the best of our knowledge, no paper reporting the preparation of Pd-Ni composite material using Ni_2O_3 as the nickel source was published so far.

Besides the chemical compositions, the morphology of an electrocatalyst was also an important factor which could greatly affect the electrocatalytic activity of the studied electrocatalyst towards an electrochemical reaction. That is to say, Pd-Ni composite catalysts with various morphologies were urgently prepared in recent years so as to further increase their electrocatalytic activities. For example, Nguyen's group [26] prepared a Pd-coated Ni nanowire catalyst via a two-step process in a polyol medium in which $NiCl_2$ and N_2H_4 were respectively utilized as the nickel source and reducing agent. Lu's group [27] prepared spherical palladium nanoparticles, reduced graphene oxide and polydopamine (PDA) onto a three-dimensional nickel foam substrate (Pd/rGO/PDA@NF) forming a novel morphology of Pd-Ni composite catalyst which showed excellent electrocatalytic activity for EOR. Yavari [28] prepared nano raspberry-like palladium particles onto the spongy nickel oxides (SNO) generating a particular morphology which delivered an evident catalytic activity towards EOR. In Yavari's work [28], SNO was synthesized by a solution combustion method, and Pd particles were prepared by a conventional chemical reduction where Pd^{2+} and $NaBH_4$ were respectively employed as the Pd source and the strong reducing agent. Wu's group [29] synthesized Pd@PtNi multimetallic nanorings through the selective epitaxial growth of Pt alloyed shells on the periphery of Pd nanoplates in which all prepared samples exhibited remarkably enhanced activity and stability for EOR. Although many novel shapes of Pd-Ni composite catalysts, including the earlier mentioned configuration of core-shell nanoplate [23] and nanotube [24], have been developed lately, the preparation of Pd-Ni composite catalysts constructed by huge spherical particles and sawdust-shaped particles is rarely reported, to our knowledge.

In this work, a precursor containing NiO and carbon material was firstly prepared via a hydrothermal process assisted air calcination approach in which Ni_2O_3 and glucose were utilized as the starting materials. During the preparation process of the precursors, four different amounts of Ni_2O_3 were added while keeping the concentration of glucose unchanged, correspondingly, generating four

kinds of precursors. Secondly, one resultant precursor and PdO reacted fully in a well-sealed high pressure reactor to complete the hydrothermal process. Thus, four types of composite catalysts were prepared. As indicated by the SEM images, huge spherical particles and regular particles, huge spherical particles and sawdust-shaped particles were, respectively, presented in catalyst c_0 and c_1. In contrast, only some agglomerates assembled by powder-shaped particles powder were exhibited distinctly in both c_2 and c_3. Mostly importantly, compared with the Ni free catalyst (catalyst c_0), all newly prepared Pd-Ni composite catalysts (catalyst c_1, c_2 and c_3) delivered a significantly increased electrocatalytic activity towards EOR. Apparently, compared with the previous works concerning Pd-Ni composite catalysts, except for Ni, Pd, O and C, no other elements as impurities were introduced into the target catalysts, which was the most distinguishing feature of this work relative to other works regarding Pd-Ni catalysts reported previously. Showing the successful preparation of a Pd-Ni composite catalyst containing huge spherical particles and sawdust-shaped particles through a two-step approach using Ni_2O_3 and glucose and $PdO \cdot H_2O$ as the starting materials was the main dedication of this preliminary work, which was very meaningful to the progress of EOR Pd-Ni composite catalysts, owing to the cost effective preparation procedure and the significant EOR electrocatalytic activity as well.

2. EXPERIMENTAL DETAILS

2.1 Reagents and materials

All chemical agents like glucose, Ni_2O_3 and $PdO \cdot H_2O$ were bought from Tianjin Yongda Chemical Reagent Co., Ltd (China) and used as received with no further treatments. All electrodes employed in this work were purchased from Tianjin Aida Co., Ltd (China). The electrolyte solution containing 1 M KOH and 1M ethanol was carefully prepared by using secondary distilled water.

2.2 Fabrication of Pd-Ni composite catalysts

The preparation of Pd-Ni composite catalysts was conducted through the following two steps. Firstly, a precursor containing NiO and carbon material was prepared using a hydrothermal process assisted air calcination method. Namely, 15 mL of 0.5 M glucose and 0.05 g of Ni_2O_3 solid powder were placed together in a home-made high pressure autoclave generating a suspension solution. And then, above well sealed autoclave was heated at 180 ºC in a drying box for 10 h to end the hydrothermal process. Subsequently, after being cooled down to the room temperature, the suspension solution in above autoclave was carefully filtered so as to harvest some solid residues. And promptly, the obtained solid residues were rinsed by double distilled water for three times in a suction filtration device to yield a well cleaned sample. Soon afterwards, the obtained sample was dried in a drying box at 70 ºC for 8 h to produce a well dried sample. Finally, the obtained sample was calcined under air atmosphere at 500 ºC in a muffle furnace for 2 h to prepare the final precursor (denoted as precursor p_1). Besides the added amount of Ni_2O_3, the preparation conditions of other samples were the same as

that of preparing precursor p_1. That is, the samples fabricated in the presence of 0 g, 0.05 g, 0.10 g and 0.15 g of Ni_2O_3, were identified as precursor p_0, p_1, p_2, and p_3, respectively.

In preparing the final catalysts, a hydrothermal process was also employed. Namely, 15 mg of p_0 and 15 mg of $PdO{\cdot}H_2O$ were put together in a centrifugal tube and dissolved in 3.5 mL double distilled water generating a suspension solution which was subjected to 70 min ultra-sonication treatment so as to form a more uniform suspension solution. After that, the resultant suspension solution was transferred into a home-made autoclave. And in the meantime, the used centrifugal tube was carefully rinsed by double distilled water for two times. It should be emphasized that all the solutions (about 6.5 mL) used for rinsing above centrifugal tube were totally transferred into above home-made autoclave. Next, the home-made autoclave was well-sealed and heated in a drying box at 200 ºC for 3 h to accomplish the hydrothermal process. The following processes for fabricating other final samples were the same as that for preparing above precursor. The final samples prepared using p_0, p_1, p_2 and p_3 were, respectively, nominated as catalyst c_0, c_1, c_2 and c_3.

2.3 Preparation of as-prepared catalysts modified GC electrodes

Firstly, 1.5 mg of c_0 was dissolved in 0.5 mL of Nafion ethanol solution (in the Nafion ethanol solution, the mass content of Nafion was about 0.1 wt.%) generating a black suspension solution, immediately, the resultant suspension solution was treated by ultrasonic oscillation at room temperature for 70 min to form a catalyst ink. Soon afterwards, 16 μL of above catalyst ink was cautiously added drop wise onto a cleaned glassy carbon (GC) electrode (The diameter of the GC electrode cross section was 3 mm). Lastly, above catalyst modified electrode was dried naturally in the air atmosphere for 12 h to produce the final catalyst c_0 modified GC electrode. The GC electrodes modified with catalyst c_0, c_1, c_2 and c_3 were called as electrode e_0, e_1, e_2 and e_3, respectively.

2.4 Characterization

The crystalline phase and chemical components of all prepared samples were thoroughly examined by using X-ray diffraction (XRD, Bruker D8 ADVANCE X-ray diffractometer equipped with a Cu Kα source (λ = 0.154 nm) at 40 kV and 30 mA). The surface morphologies of all prepared samples were thoroughly observed by using scanning electron microscopy (SEM, HITACHI, S-570). The surface morphology of catalyst c_1 was also viewed by using transmission electron microscopy (TEM, HITACHI, H-7650). The element contents of all as-synthesized catalysts were examined by using energy dispersive X-ray spectroscopy (EDS, PV-9900, USA). Fourier transform infrared spectrometry (FTIR) of all studied samples was carried out on a Hitachi FTIR-8900 spectrometer (Japan) with an intention to ascertain the functional groups existing in all studied samples. To exactly determine the chemical compositions of all as-prepared catalysts, the valences of the elements existing in the prepared catalysts were detected by using X-ray photoelectron spectroscopy (XPS, Kratos Analytical spectrometer, Al K_α radiation).

The typical electrochemical measurements such as CV (Cyclic voltammetry), CA

(Chronoamperometry) and EIS (Electrochemical impedance spectroscopy) were all performed on an electrochemical workstation (CHI 660E, Shanghai Chenhua Apparatus, China) via a conventional three-electrode cell. In the traditional three-electrode cell, the catalyst coated GC electrode, a Pt (platinum) foil and a SCE (saturated calomel electrode) were, respectively, used as the working, auxiliary and reference electrode. That is to say, all potential values appearing in this work were referred to the electrode potential value of SCE. The solution containing 1M KOH and 1M ethanol was employed as the electrolyte solution via which the electrocatalytic activities of all prepared catalysts towards EOR were fully investigated. All the aqueous solutions were prepared by using double distilled water and all measurements were performed at room temperature with no special inert gas protection.

3. RESULTS AND DISCUSSION

3.1 Characterizations of all prepared samples

XRD patterns of all as-synthesized precursors are given in Fig.1a. For precursor p_0, only a broad and weak diffraction peak was clearly exhibited in the 2θ region ranging from 20° to 30° which was generally attributed to the presence of carbon material [30].

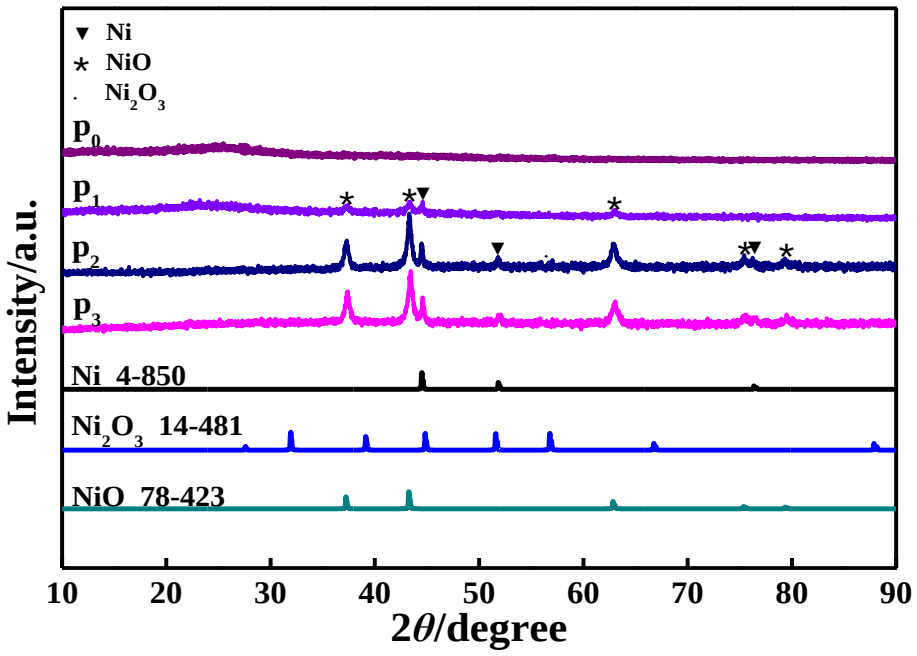

Figure 1a. XRD patterns for all prepared precursors in which the standard XRD patterns for Ni, NiO and Ni_2O_3 were all presented. Pattern p_0, p_1, p_2 and p_3 corresponded to precursor p_0, p_1, p_2 and p_3.

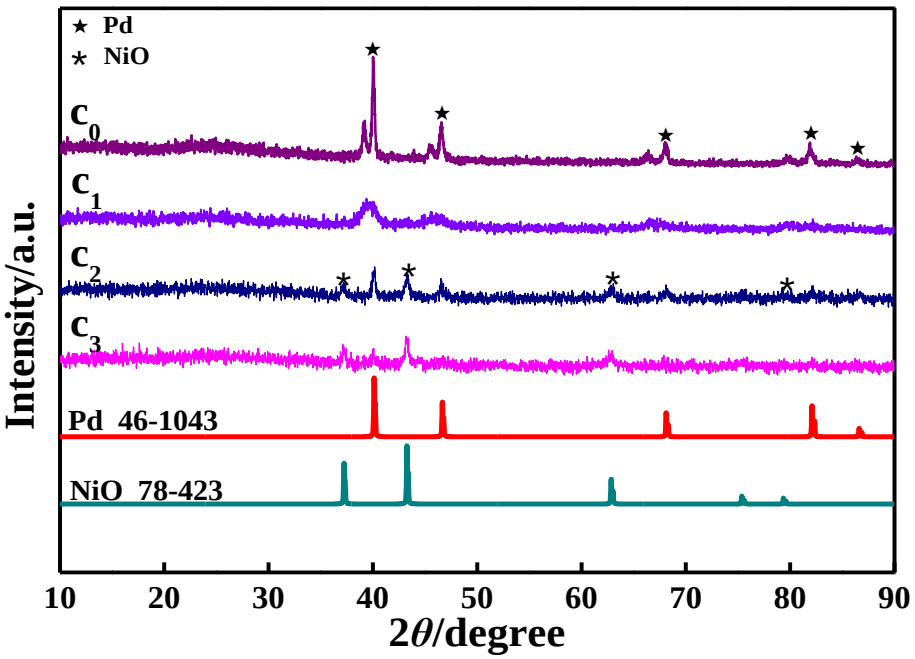

Figure 1b. XRD patterns for all as-synthesized catalysts as well as the standard patterns of Pd and NiO. Pattern c_0, c_1, c_2 and c_3 corresponded to catalyst c_0, c_1, c_2 and c_3.

Interestingly, for other three precursors, several evident and sharp diffraction peaks were definitely displayed which strongly indicated that some substances with higher crystallinities were present in the as-prepared precursors. More precisely speaking, in the XRD patterns of precursor p_1, p_2 and p_3, the diffraction peaks located at 2θ angle of 37.2°, 43.4° and 62.9° were, respectively, assigned to the crystal plane (111), (200) and (220) of NiO (JCPDS, NO.78-423) [31] indicating the successful preparation of NiO in the resultant precursors. Particularly, in the case of precursor p_2 and p_3, other two typical diffraction peaks respectively positioned at 75.4° (311) and 79.4° (222) were also distinctly exhibited further confirming the existence of NiO [31]. Also, as shown by the black solid inverted triangle symbol, three characteristic diffraction peaks indexed as the crystallographic plane (111), (200) and (220) of metallic Ni (JCPDS,NO.4-850) [32] were also observed at 2θ angle of 44.6°, 51.8° and 76.3°, respectively, corroborating the presence of metallic Ni in precursor p_1, p_2 and p_3. Interestingly, the diffraction peaks attributable to Ni_2O_3 almost vanished in above three precursors suggesting that the added Ni_2O_3 was totally reduced during the preparation process. That is, the added Ni_2O_3 has fully reacted with glucose in the first hydrothermal process generating a compound that contained NiO and carbon materials, and then, in the air calcination process, part of the resultant NiO was further chemically reduced by the prepared carbon materials (In above hydrothermal process, a large number of huge carbon spheres would be prepared based on the previous work [33]) giving birth to the metallic Ni. Or in other words, carbon materials were excessive as compared to the added amount of Ni_2O_3. As a result, no residual Ni_2O_3 was left in the prepared precursors. Thus, it was inferred, based on the XRD patterns shown in Fig.1a, that NiO and carbon materials were the main components of p_1, p_2 and p_3 though a very little amount of metallic Ni was also present.

XRD patterns of all prepared catalysts are illustrated in Fig.1b. For catalyst c_0, namely, the

catalyst prepared using precursor p_0, five evident diffraction peaks centered at 2θ angle of 40.0°, 46.5°, 68.1°, 81.9° and 86.5° were (as shown by the large solid five-pointed star), respectively, assigned to the crystal plane (111), (200), (220), (311) and (222) of the face centered cubic metallic Pd (JCPDS, NO. 46-1043) [34] indicating the successful preparation of metallic Pd in c_0. Apparently, above five diffraction peaks were all visible in catalyst c_1, c_2 and c_3, which strongly indicated that metallic Pd as one main component also existed in all prepared Pd-Ni catalysts. In the XRD patterns of catalyst c_1, c_2 and c_3, three small evident diffraction peaks assigned to crystal plane of (111), (200) and (220) of NiO [31] were, respectively, positioned at 2θ angle of 37.2°, 43.4° and 62.9°, substantially indicating that NiO as one main substance still remained in all prepared Pd-Ni catalysts. Summarily, as revealed by the XRD patterns, metallic Pd and NiO as two main substances existed in catalyst c_1, c_2 and c_3.

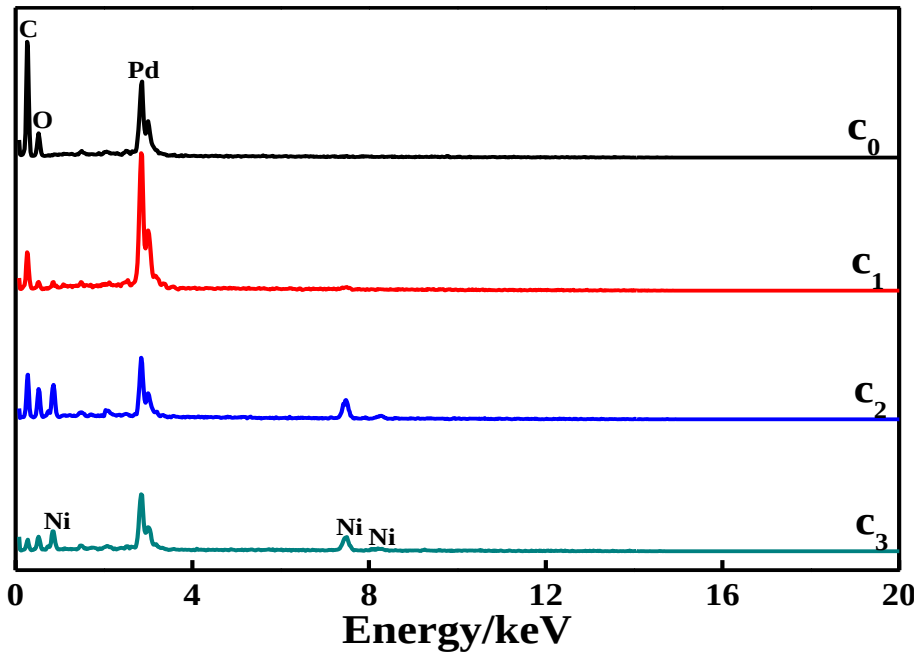

Figure 2a. EDS patterns for all as-prepared catalysts. Pattern c_0, c_1, c_2 and c_3 corresponded to catalyst c_0, c_1, c_2 and c_3.

EDS patterns of all prepared catalysts are presented in Fig.2a. For c_0, only the peaks belonging to element C, O and Pd were exhibited in which the atomic contents of C, O and Pd were, respectively, examined to be 54.8%, 34.0% and 11.2%. While, for other three catalysts, besides above three elements, the peaks assigned to element Ni were also displayed clearly indicating that catalysts c_1, c_2 and c_3 were a Pd and Ni composite material. The atomic contents of Ni and Pd in catalyst c_1, c_2 and c_3 were approximately measured to be 3.3% and 35.5%, 25.0% and 14.6%, 27.2% and 21.8%, respectively. That is, catalyst c_1 had the largest atomic content of Pd among all prepared catalysts. The atomic contents of C and O were, respectively, roughly detected to be 36.9% and 24.3%, 11.3% and 49.1%, 8.3% and 42.8% in catalyst c_1, c_2 and c_3. Evidently, the atomic content of C in above three catalysts decreased with increasing the added amount of Ni_2O_3. Probably, the following two reasons

were responsible for above decreasing trend of carbon content, firstly, during the air calcination procedure for preparing the precursors, more amounts of carbon materials would be used to react with Ni_2O_3 via the following chemical reaction, namely, $C+Ni_2O_3 \rightarrow$ CO (or CO_2) +NiO, thus, with increasing the added amount of Ni_2O_3, less amount of carbon material was maintained in the prepared precursor. Next, in the second hydrothermal process of preparing the final catalysts, probably, the carbon materials of the precursors reacted with PdO to yield metallic Pd on the basis of the following chemical reaction, i.e., $C+PdO \rightarrow$ CO (or CO_2) +Pd, further reducing the carbon content in the final catalysts. In a nutshell, the amount of carbon consumed would increase obviously with increasing the added amount of Ni_2O_3, as a result, catalyst c_3 had the minimum atomic content of carbon among above three Pd-Ni catalysts. As a representative, the EDS mapping images of catalyst c_1 are shown in Fig.2b in which the EDS mappings for element C, O, Ni and Pd are all clearly presented. Particularly, for the EDS mapping of element Pd, a large number of red dots were uniformly scattered in the whole observation window indicating that element Pd had a homogeneous distribution in catalyst c_1, which was very beneficial to the full contact between the electroactive molecules (here ethanol molecules were the electroactive molecules) and the employed catalysts.

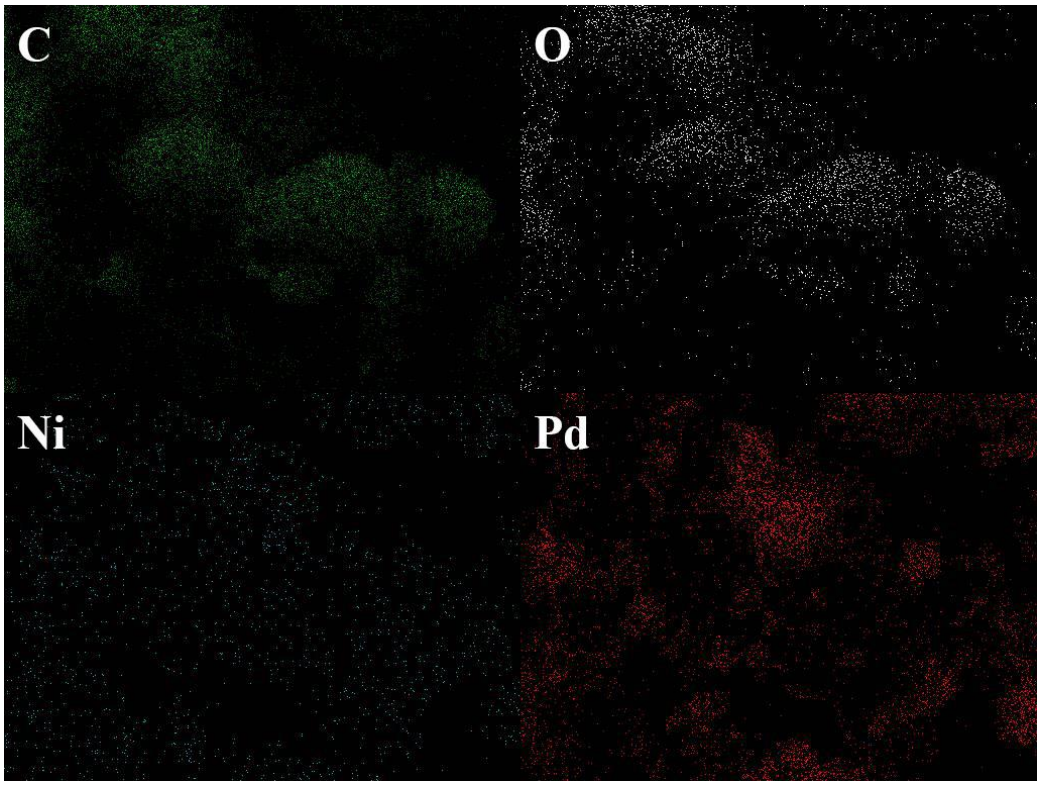

Figure 2b. EDS mapping images for catalyst c_1 in which the EDS mapping image of element C, O, Ni and Pd were all well displayed.

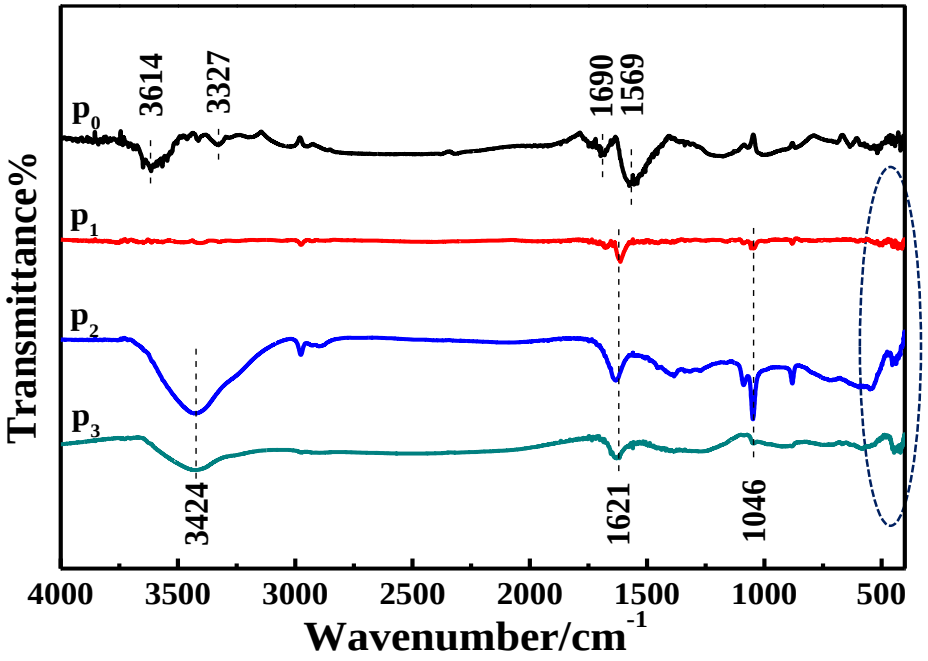

Figure 3a. FTIR spectra for all as-prepared precursors. Curve p_0, p_1, p_2 and p_3 corresponded to precursor p_0, p_1, p_2 and p_3.

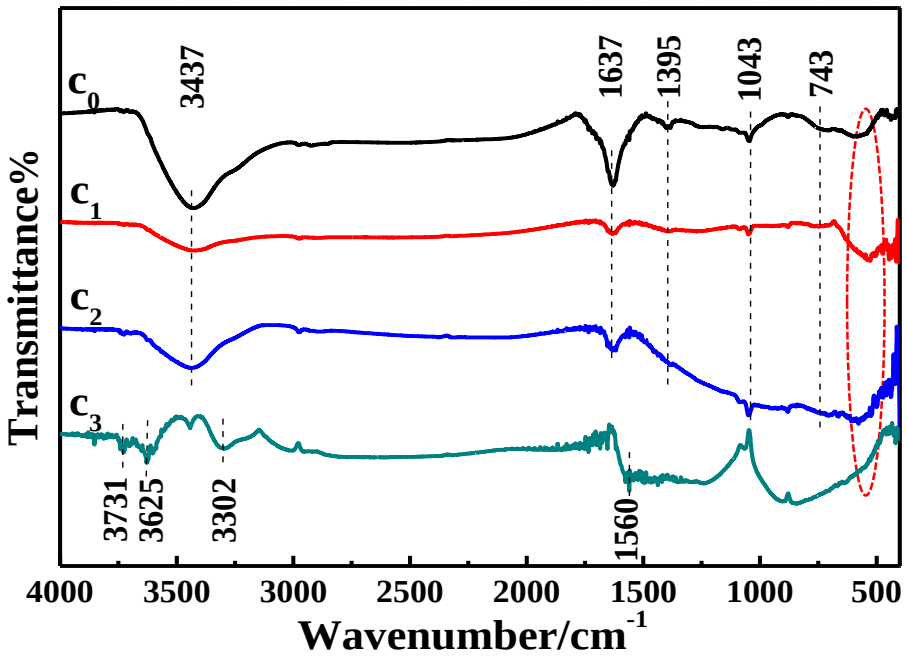

Figure 3b. FTIR spectra for all as-prepared catalysts. Curve c_0, c_1, c_2 and c_3 corresponded to catalyst c_0, c_1, c_2 and c_3.

FTIR spectra for the precursors are shown in Fig.3a. In the FTIR spectra for p_0, the absorption peak positioned at 3614 cm^{-1} should be originated from the presence of O-H bending vibrations [35].

The absorption peaks successively appearing at 1569 and 1690 cm^{-1} were reported to be attributed to C=C [36] and C=O vibrations[36], respectively, further authenticating the aromatization process of glucose based on the previous work [33]. For the FTIR patterns of p_2 and p_3, the absorption bands positioned at 1046 and 1621 cm^{-1} were reported to be originated from the C-O and C=O stretching vibrations [37], respectively. As shown by the black circled part, the broad absorption peaks at 442 cm^{-1} and 446 cm^{-1} should, respectively, be assigned to the NiO vibration in p_2 and p_3 [38]. To one's surprise, for precursor p_1, the huge absorption band located at about 3424 cm^{-1} totally vanished, and the intensity of the absorption band at 1621 cm^{-1} became weaker as compared to that of p_2. Also for precursor p_1, a small absorption band at 507 cm^{-1} was displayed clearly which was generally attributable to the Ni-O bond vibration [39, 40]. That is to say, the results of FTIR shown in Fig.3a further demonstrated that carbon materials and NiO were the main substances of precursor p_1, p_2 and p_3, being well in accordance with the XRD analysis (Fig.1a).

FTIR spectra of all as-prepared catalysts are given in Fig. 3b. Evidently, similar shape of the FTIR spectra was displayed by catalyst c_0, c_1 and c_2 which strongly indicated that identical organic functional groups existed in the as-studied catalysts. As shown by the red circled part, a broad absorption peak centered at about 540 cm^{-1} was distinctly presented in the FTIR spectra of catalyst c_0, c_1 and c_2, which were generally reported to be the typical absorption band of NiO [41]. In the case of c_3, as compared to other catalysts, the intensities of the absorption peaks at 3437 cm^{-1} and 1637 cm^{-1} attenuated remarkably indicating that less amount of carbon was contained in catalyst c_3, which accorded well with the EDS result (Fig.2a) (the atomic content of carbon in c_3 was as low as 8.3%). Even so, three absorption peaks (respectively at 3731, 3625 and 3302 cm^{-1}) assigned to the O-H vibrations [42] were all evidently displayed in the FTIR spectrum of c_3. That is to say, the surfaces of all prepared catalysts were fully covered by the hydrophilic -OH groups which was very conducive to the direct contact between ethanol molecules and catalysts.

XPS spectra of c_1, c_2 and c_3 are presented in the figures of Fig.4 desiring to further ascertain the chemical compositions of all prepared Pd-Ni catalysts through detecting the chemical valence of the elements existing in the studied samples. In Fig. a (the wide scan XPS spectra), the peaks assigned to the element Ni, O, Pd and C were all exhibited clearly which was consistent with the EDS result (Fig.2a). In the C1s XPS spectra (Fig. b), four binding energy (BE) peaks were displayed obviously in the pattern of c_1 suggesting that at least four kinds of carbon atoms existed in c_1. More specifically, the BE peaks located at 284.5, 286.3, 288.2 and 290.0 eV were, respectively, attributed to the carbon of sp^2-C [43], C-OH [44], C=O [45] and CO_3^{2-}[46]. In the case of catalyst c_3, the BE peaks appearing at both 288.2 eV and 290.0 eV almost vanished, and the intensity of the BE peak assigned to sp^2-C (at 284.5 eV) was evidently lower than that of c_1 and c_2, which should be mainly attributed to the lower content of carbon in c_3 (Fig.2a).

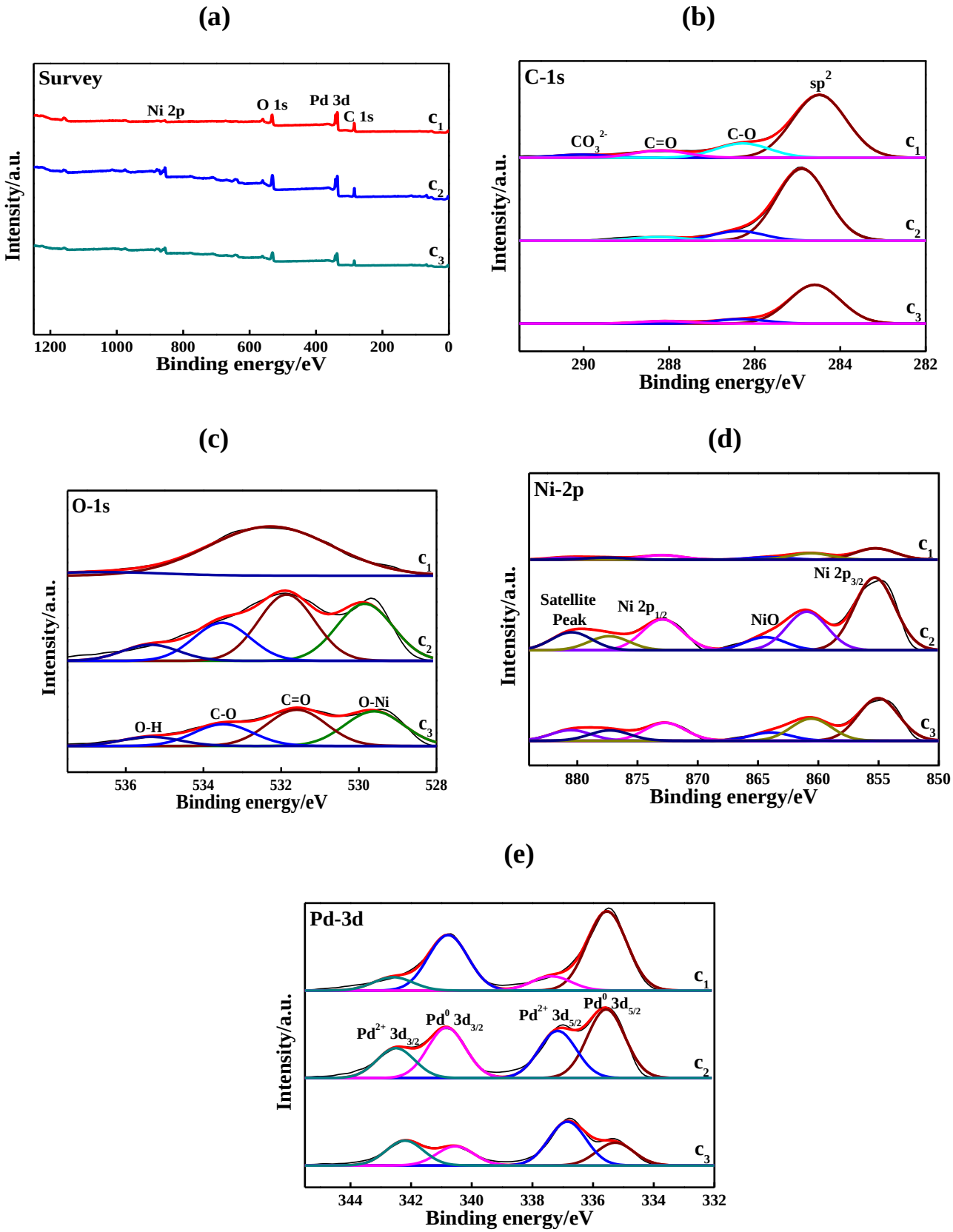

Figure 4. XPS survey spectra for all prepared Pd-Ni catalysts in which curve c_1, c_2 and c_3 corresponded to catalyst c_1, c_2 and c_3. **(a)** Wide scan XPS survey spectra; **(b)** C1s spectrum of XPS spectra; **(c)** O1s spectrum of XPS spectra; **(d)** Ni 2p spectrum of XPS spectra; **(e)** Pd 3d spectrum of XPS spectra.

In addition, compared to BE peak assigned to sp^2-C of catalyst c_1, the BE peak positions of carbon assigned to sp^2-C for c_2 and c_3 were positively shifted for about 0.3 eV and 0.1 eV, respectively, which was generally due to the chemical environment variation of carbon element in the studied samples. The O1s XPS spectra for all studied catalysts are displayed in Fig. c. For catalyst c_1, only a huge and broad BE peak centered at 532.4 eV, that was usually assigned to O1s of -OH [44], was exhibited in the whole binding energy testing period. While for c_2, four BE peaks successively located at 529.8, 531.8, 533.6 and 535.5 eV were explicitly displayed, respectively, corresponding well to the O1s of Ni-O [47], C=O [44], HO-C=O [44] and -OH [48]. The Ni2p XPS spectra for all as-studied catalysts are given in Fig. d. Apparently, the intensities of BE peaks for catalyst c_1 were evidently lower than that for catalyst c_2 and c_3 which strongly indicated that less amount of Ni-containing substance was contained in c_1. For c_2, the BE peak at 855.4eV along with its satellite peak at 861.0 eV [49] and the BE peak at 873.1eV along with its corresponding satellite peak at 880.6 eV [50] were, respectively, assigned to the core energy level spectrum of Ni $2p_{3/2}$ and Ni $2p_{1/2}$, substantially indicating the presence of Ni^{2+} in c_2.

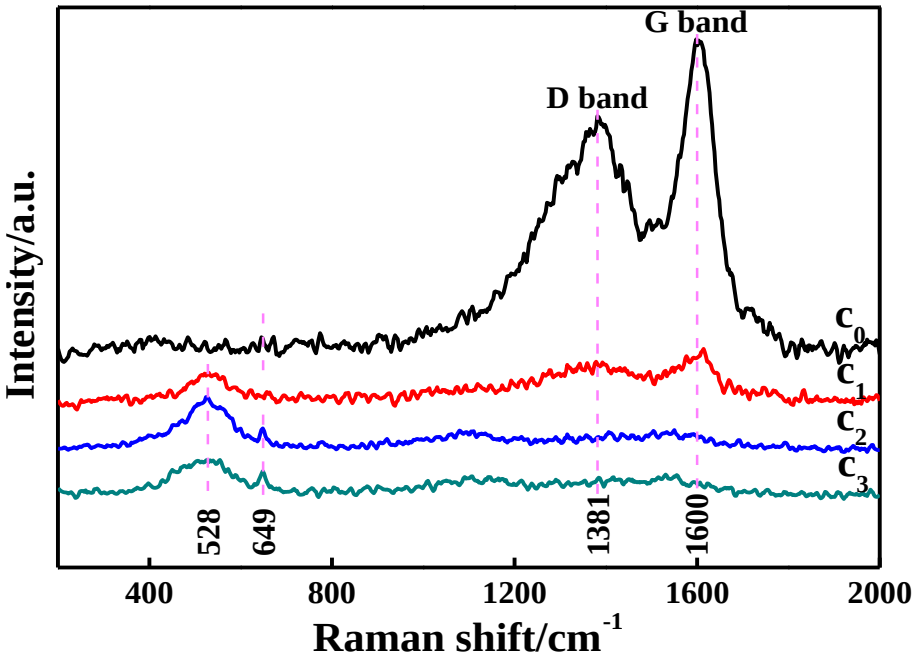

Figure 5. Raman spectra for all synthesized catalysts in which curve c_0, c_1, c_2 and c_3 corresponded to catalyst c_0, c_1, c_2 and c_3.

Also, the main characteristic BE peak at 853.1 eV indexed as metallic Ni [51] was not found in Fig.d indicating the absence of metallic Ni in the studied catalysts, which was well consistent with the XRD results (Fig.1b). The high resolution Pd XPS spectra for all studied catalysts are shown in Fig. e of Fig.4 in which four BE peaks were clearly exhibited in each XPS spectrum. Generally, the BE peaks at 335.5 eV and 337.3 eV were respectively assigned to the $3d_{5/2}$ orbit of Pd^0 [52] and Pd^{2+} [53], and

the BE peaks appearing at 340.8 eV [52] and 342.6 eV [53] were respectively originated from the orbit of Pd^0 ($3d_{3/2}$) and Pd^{2+} ($3d_{3/2}$). Obviously, in the case of catalyst c_1, the intensity of the BE peak assigned to Pd^0 was significantly higher than that of the BE peak assigned to Pd^{2+}. That is, more amount of metallic Pd was prepared in catalyst c_1 which accorded well with the XRD results (Fig.1b). Approximately, on the basis of the XPS analysis, the atomic contents of Pd^0 and Pd^{2+} in c_1, c_2 and c_3 were measured to be 83.0% and 17.1%, 60.7% and 39.5%, 38.2% and 62.1%, respectively. Thus, also being combined with the XRD analysis results (Fig.1b), it was concluded that catalyst c_1 had the largest amount of metallic Pd among above three prepared catalysts. That is to say, carbon material, metallic Pd, NiO and PdO were all contained in the prepared catalysts of c_1, c_2 and c_3.

Raman spectra for all prepared catalysts are given in Fig.5. For catalyst c_0, namely, the catalyst prepared in the absence of Ni_2O_3, two huge characteristic peaks attributed to the carbon material were displayed clearly. According to the previous work [54], the peaks located at 1600 cm^{-1} and 1381 cm^{-1} were, respectively, assigned to the graphitic band (G-band) and disorder band (D-band) of carbon material. And for c_0, the intensity ratio of D- to G-band (I_D/I_G) was about 0.75, which strongly indicated that the carbon material present in c_0 had a relatively higher degree of crystallinity. For other three catalysts, above two peaks as small peaks were also clearly exhibited indicating that carbon material as one main substance was still present in catalyst c_1, c_2 and c_3. The intensity ratios of I_D/I_G for c_1, c_2 and c_3 were roughly estimated to be 0.74, 0.98 and 0.90, respectively. Thus, c_1 showed the best ordered graphitic nature [55, 56] among above three Pd-Ni catalysts which, based on our work [57], was advantageous to the orderly transfer of electrons. In addition, in the case of catalyst c_1, c_2 and c_3, an evident broad peak centered at 528 cm^{-1} was exhibited clearly, which was an evidence of the presence of NiO [58]. Also, a very small peak at 649 cm^{-1} was observed in the Raman spectra of c_0, c_2 and c_3, which was generally ascribed to the presence of Pd-O bond [59, 60]. As shown by the XRD and XPS patterns, metallic Pd as the main Pd-containing substance was present in catalyst c_1, therefore, the small peak at 649 cm^{-1} indexed as Pd-O bond was not observed in the Raman spectra of c_1. Thus, the results of Fig.5 substantially demonstrated that all prepared catalysts were a composite material rather than a pure substance, which was well consistent with the aforementioned measurement results.

3.2 SEM characterization

SEM images with a scale of 2 μm of all prepared precursors are shown in Fig.6a. For precursor p_0, besides some smaller particles, a well-defined spherical particle with a diameter of about 4.5 μm was clearly exhibited. It strongly indicated that some spherical particles were still remained in precursor p_0 even after the 500 ºC calcination process.

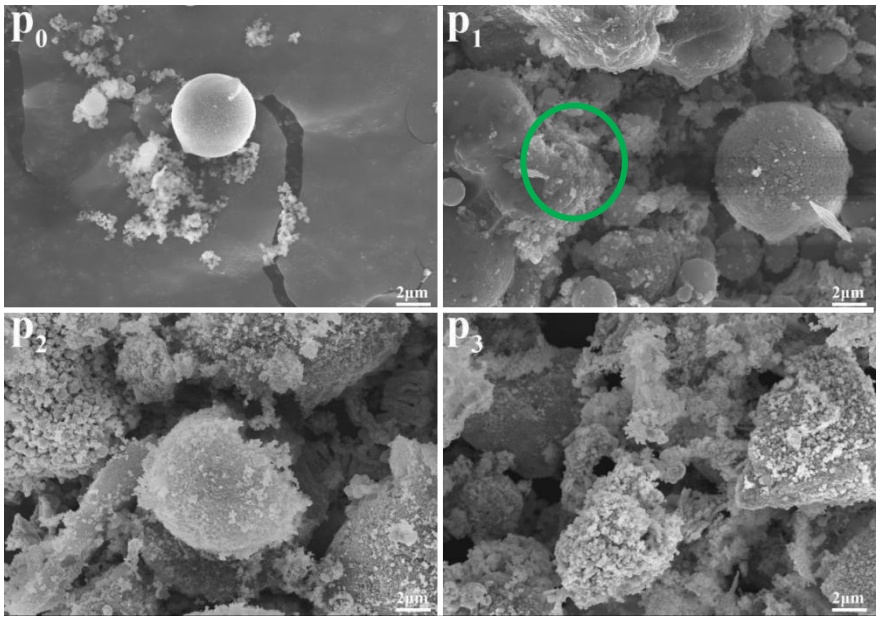

Figure 6a. SEM images with a scale of 2 μm for all prepared precursors. Image p_0, p_1, p_2 and p_3 corresponded to precursor p_0, p_1, p_2 and p_3.

(a)

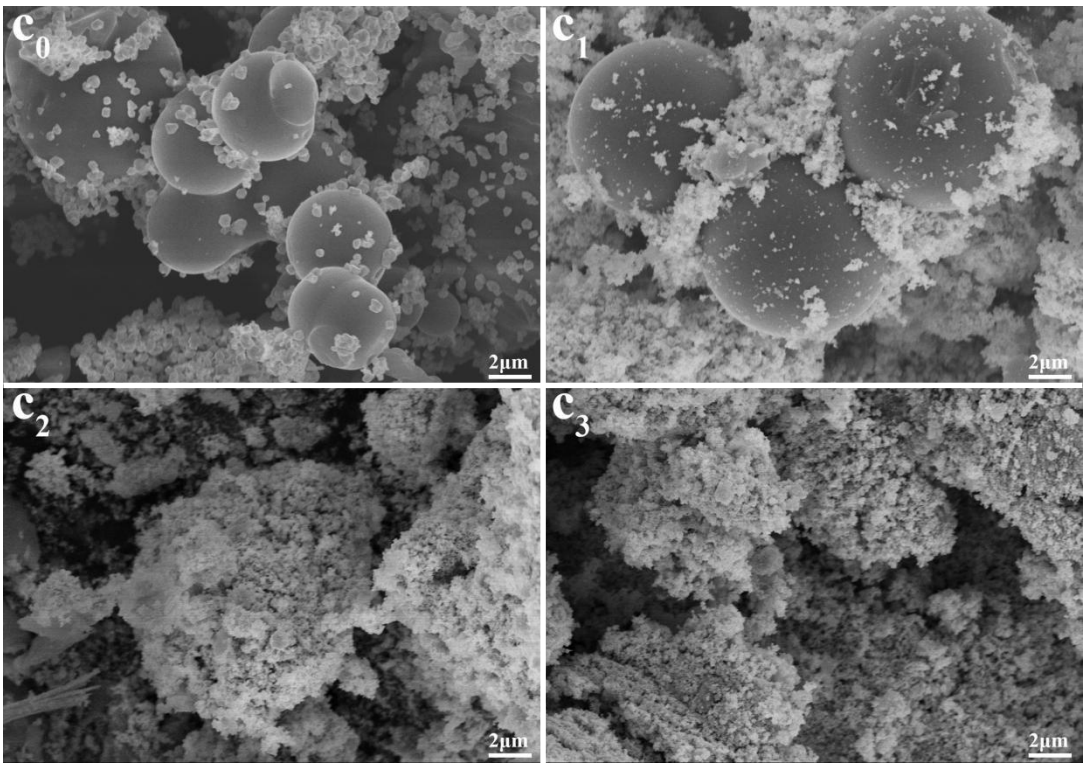

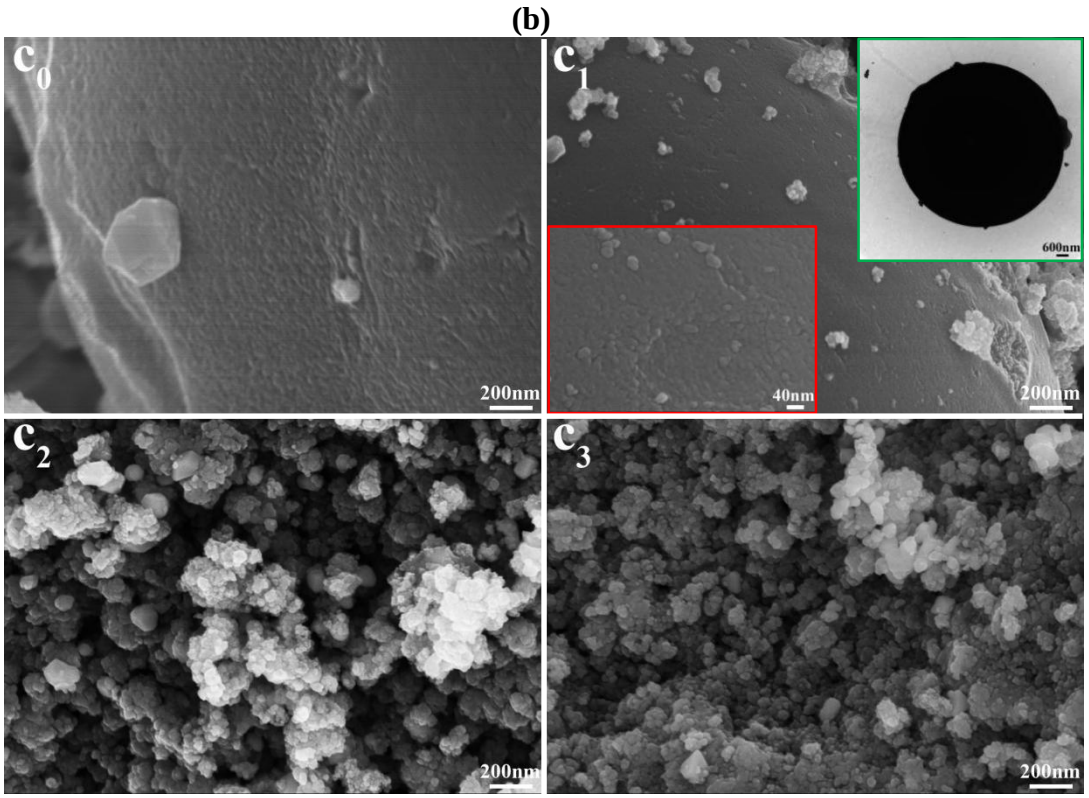

Figure 6b. SEM images with various scales for all prepared catalysts. Image c_0, c_1, c_2 and c_3 corresponded to catalyst c_0, c_1, c_2 and c_3. **(a)** SEM images with a scale of 2 μm for all prepared catalysts. **(b)** SEM images with a scale of 200 nm for all prepared catalysts in which the SEM image at the left lower corner of image c_1 was the SEM image with a scale of 40 nm for the huge spherical particle surface of c_1 and the TEM image at the upper right corner of image c_1 was the TEM image with a scale of 600 nm for the huge spherical particle appearing in c_1.

For precursor p_1, several spherical particles with different sizes were clearly displayed in the observation window. As shown by the green circled part, a huge irregular particle with a layered structure was presented distinctly indicating some spherical particles formed during the hydrothermal process were totally destroyed in the calcination process. For precursor p_2, except for some huge irregular agglomerates, a broken spherical particle with a bumpy surface was seen clearly. Nevertheless, in the image of precursor p_3, no spherical particles could be seen anymore, instead, many aggregates constructed by a large number of small particles were exhibited distinctly. In a word, the morphologies of the as-prepared precursors were rather different from each other, which effectively indicated that the added amount of Ni_2O_3 in the preparing system played an important role in determining the final morphologies of the prepared precursors. The collection of the SEM images with a scale of 2 μm for all prepared catalysts is presented in figure a of Fig.6b. Apparently, besides a large number of irregular small particles, several huge spherical particles with an average diameter close to 3.5 μm were clearly displayed in c_0. By comparing with the image of precursor p_0 (Fig.6a), it could be inferred that the huge spherical particles appearing in the precursor p_0 were not damaged in the second hydrothermal process. In the case of c_1, except for several huge spherical particles with a diameter of about 9.2 μm, a lot of sawdust-shaped particles were also explicitly presented, generating a catalyst

consisting of huge spherical particles and sawdust-shaped particles. For catalyst c_2 and c_3, those huge spherical particles presented in c_0 and c_1 totally vanished, instead, a great quantity of powder-shaped particles appeared. SEM images with a scale of 200 nm of all resultant catalysts are shown in figure b of Fig.6b. As indicated by image c_0, a small and regular particle with a size of 360 nm was definitely immobilized on the surface of a huge spherical particle. While for catalyst c_1 (image c_1), the diameter of those small particles anchored on the surface of the huge spherical particles was measured only to be about 40 nm. The inserted image at the lower left corner of image c_1 was the magnified SEM image of the huge spherical particle appearing in image c_1 from which it could be seen clearly that the surface of the huge spherical particle was composed by numerous small protuberances. The inserted image at the top right-hand corner of image c_1 was the TEM image of one huge spherical particle of c_1 in which a black huge spherical particle with a well-defined spherical boundary was exhibited distinctly, which substantially indicated that all huge spherical particles appearing in c_1 were the solid particles rather than the hollow particles. For c_2, several huge hierarchical aggregates assembled by a lot of small particles were displayed distinctly where no big spherical particles were found anymore. In the case of c_3, several irregular agglomerates that were constructed by many irregular small particles were observed explicitly. That is to say, the added amount of Ni_2O_3 in preparing the precursors was a key factor which would further affect the final morphologies of all prepared catalysts.

3.3. Electrocatalytic performances of all as-prepared catalysts for EOR

The electrocatalytic performances of all as-synthesized catalysts for EOR were first studied by using cyclic voltammetry (CV) and the CV curves are compared in Fig.7a. Apparently, for all prepared catalysts, an electrochemical oxidation peak (nominated as peak f) with a peak potential of about -0.28V appeared in the positive direction potential scanning which was followed by an abnormal electrochemical oxidation peak (nominated as peak b) emerging in the negative direction potential scanning. The presence of above two typical CV peaks of EOR strongly demonstrated that all newly prepared catalysts had an evident electrocatalytic activity towards EOR. Generally, peak f and peak b corresponded to, respectively, the direct electrochemical oxidation of ethanol molecules and the electrochemical oxidation of the intermediates that were generated during the positive direction potential scanning [61]. Evidently, the peak current densities of both peak f and peak b, that were measured on the catalyst c_1, c_2 and c_3, were all significantly larger than that measured on catalyst c_0, indicating that the electrocatalytic activities of all newly prepared Pd-Ni catalysts were all superior to that of Ni free Pd-based (catalyst c_0). For example, the peak current densities of peak f measured on c_0, c_1, c_2 and c_3 were recorded to be about 0.9, 32.4, 10.5 and 14.7 mA cm^{-2}, respectively, showing an increasing order of $c_0<c_2<c_3< c_1$. Particularly, the peak current density of peak f measured on c_1 (32.4 mA cm^{-2}) was almost 36 times larger than that measured on c_0 (0.9 mA cm^{-2}). In addition, the ratios of peak current density of peak f to that of peak b were approximately calculated to be 0.79, 0.74 and 0.61 for c_1, c_2 and c_3, respectively, which effectively indicated that more amounts of ethanol molecules were directly electrochemically oxidized on catalyst c_1 as compared to the case of using catalyst c_2 and c_3.

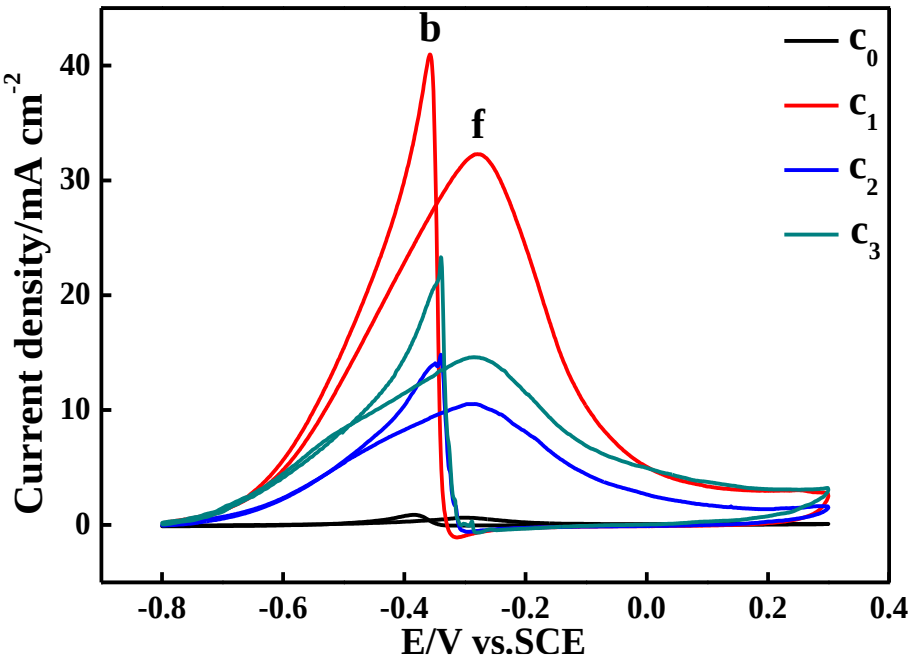

Figure 7a. Cyclic voltammetry curves recorded at 50 mV s^{-1} on different catalysts coated GC electrode in which the electrolyte contained 1M KOH and 1M ethanol. Curve c_0, c_1, c_2 and c_3 corresponded to catalyst c_0, c_1, c_2 and c_3.

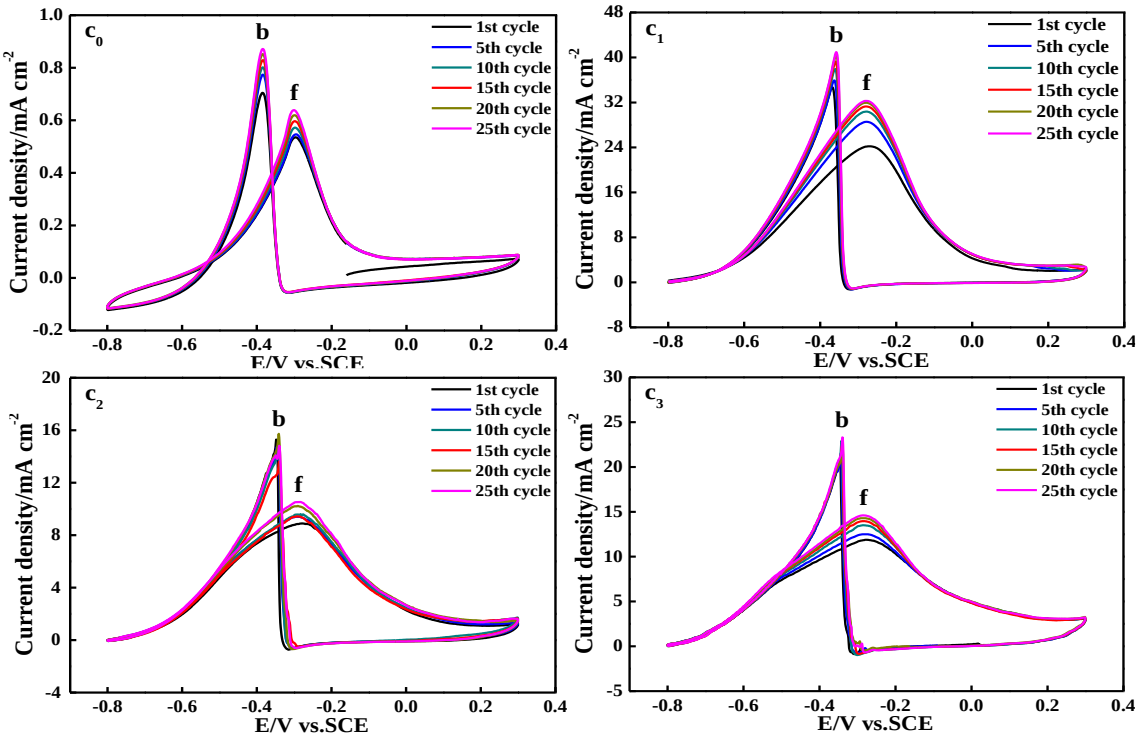

Figure 7b. Cyclic voltammetry (CV) curves measured at the 1, 5, 10, 15, 20 and 25 cycles on various catalysts coated GC electrodes in which the electrolyte was 1M KOH + 1M ethanol and the potential scanning speed was 50 mV s^{-1}. Figure c_0, c_1, c_2 and c_3 corresponded to the cases of using c_0, c_1, c_2 and c_3.

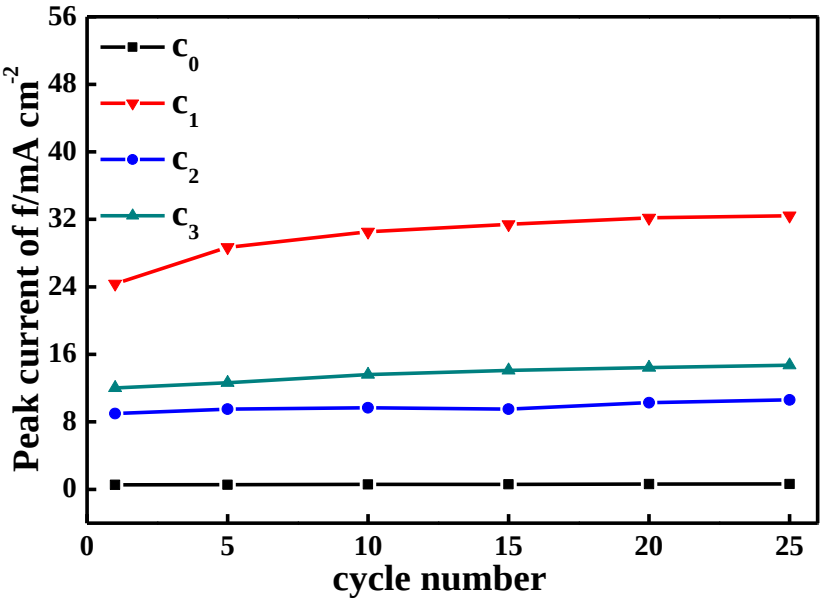

Figure 7c. The plots showing the relationship between the peak current density of the peak f for EOR and the cycling number. Curve c_0, c_1, c_2 and c_3 corresponded to the cases of using c_0, c_1, c_2 and c_3.

Meanwhile, the onset potential value of EOR measured on c_0 was negatively shifted through using the newly prepared Pd-Ni catalysts. For example, the onset potential values of peak f for catalyst c_1, c_2 and c_3 were mainly converged on the potential value of about -0.68 V, which was far negative than that of peak f for catalyst c_0 (-0.37V). That is, the over-potential of EOR on c_0 was reduced by about 310 mV via using the newly prepared Pd-Ni catalysts, which was of importance in saving the electric energy consumed for a practical EOR based fuel cell.

The cycling stabilities of all prepared catalysts towards EOR were measured and the results are given in the serial figures (figure c_0, c_1, c_2 and c_3) of Fig.7b. In this test, the CV curves of EOR on each prepared catalyst were recorded at 50 mV s^{-1} for consecutive 25 cycles. In each figure of Fig.7b, the CV curves recorded at the first, 5, 10, 15, 20 and 25 cycles were collected with an intention to identify the variation trend of the peak current density. Evidently, for each catalyst, all peak current densities for both peak f and peak b gradually increased with increasing the cycling number. As a representative, the curves showing the relationship of the peak current density for peak f and the cycle number for all studied catalysts are given in Fig.7c. Evidently, in the whole testing period, the peak current density of peak f measured on c_1 was the largest value among all measured values. For example, the peak current density value measured on the first cycle and the 25^{th} cycle for catalyst c_0, c_1, c_2 and c_3 were, respectively, 0.5 and 0.6 mA cm^{-2}, 24.2 and 32.4 mA cm^{-2}, 9.0 and 10.6 mA cm^{-2}, 11.9 and 14.5 mA cm^{-2}. It was worth emphasizing that even after 25 cycles, the peak current density of peak f on c_1 was still maintained to be as high as about 32.4 mA cm^{-2}, which was significantly higher than that measured on c_0.

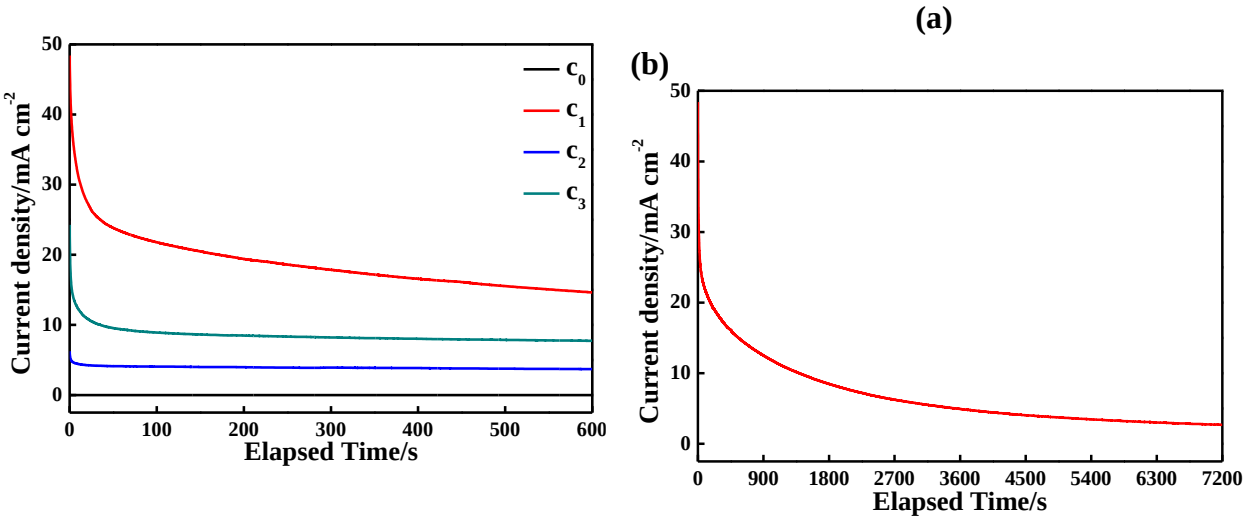

Figure 8. Chronoamperometry (CA) curves measured in the electrolyte solution consisting of 1M KOH and 1M ethanol. In this experiment, the electrode potentials of all studied working electrodes were kept at a potential value of -0.30 V. **(a)** CA curves of EOR on various catalysts coated GC electrode in which the testing time was 600 s. Curve c_0, c_1, c_2 and c_3 corresponded to the cases of using c_0, c_1, c_2 and c_3. **(b)** CA curves of EOR on catalyst c_1 coated GC electrode in which the testing time was 7200 s.

The electrocatalytic durability of a catalyst was an important parameter which was closely related to its service life in a practical cell. Thus, the electrocatalytic durability of all prepared catalysts towards EOR was also examined by using chronoamperometry (CA) and the results are shown in the figures of Fig.8. It should be noted that the electrode potentials of all studied electrodes were kept to be a constant value of -0.30 V while recording the CA curves. As shown in figure a of Fig.8, all CA curves were constructed by a rapid attenuation region and a relatively stable region. Generally, the rapid drop region of the current density appearing in the starting measurement period was originated from the capacitive current, and the relatively stable region of the current density (also called as the polarized current density or faradaic current density) was mainly resulted from the direct electrochemical oxidation of ethanol molecules [30]. Evidently, in the whole examining region, the largest polarized current density was delivered by catalyst c_1, indicating that catalyst c_1 had the best electrocatalytic durability among all studied catalysts. For example, the polarized current density values at 600 s measured on c_0, c_1, c_2 and c_3 were detected to be about 0.2, 14.7, 3.9 and 7.7 mA cm^{-2}, respectively, showing an increasing order of $c_0<c_2<c_3< c_1$. It is worth mentioning that the values of both 14.7 and 7.7 mA cm^{-2} were all remarkably higher than the reported value of 5 mA cm^{-2} [62]. That is, the electrocatalytic activities of c_1 and c_3 for EOR were significant as compared to the formerly synthesized catalyst. Apparently, the polarized current density value at 600 s measured on c_0 almost disappeared. While for catalyst c_1, c_2 and c_3, a relatively higher polarized current density value was retained even after 600 s which strongly indicated that the existence of NiO was very beneficial to the electrocatalytic durability enhancement of catalyst c_0. Further, as the testing period was prolonged to be 7200 s (figure b of Fig.8), the polarized current density value measured on c_1 was still kept to be about as high as 2.68 mA cm^{-2}. In 2020, Silva's group[63] synthesized biocarbon-supported Ni@Pd

core-shell particles and thoroughly investigated their electrocatalytic activities towards EOR reporting that in the CA test the polarized current density value measured on the as-prepared catalyst was about 12 A m^{-2} (1.2 mA cm^{-2}) at 7200 s. That is to say, the electrocatalytic activity for EOR exhibited by catalyst c_1 was superior to that of the previously synthesized catalyst [63].

The CV curves of all prepared catalysts in 1M KOH, as shown by Fig.9, were also recorded with an intention to further investigate the electrocatalytic mechanisms of all studied catalysts towards EOR. Apparently, almost no CV peaks were displayed in the case of using catalyst c_0 suggesting that the signals of electrochemical reactions were too weak to be detected. In contrast, for catalyst c_1, c_2 and c_3, an evident electrochemical reduction peak was displayed clearly at about -0.40 V which was generally ascribed to the electrochemical reduction of PdO to prepare metallic Pd, i.e., $PdO + H_2O + 2e^- \leftrightarrow Pd + 2OH^-$ [61]. Obviously, among all studied catalysts catalyst c_1 showed the largest peak current density value indicating that the largest amount of metallic Pd was formed in c_1 when the electrode potential of the working electrode approached -0.4 V. Noticeably, the increasing sequence of the peak current density value for above huge electrochemical reduction peak was as follows, namely, $c_0<c_2<c_3< c_1$, which was well consistent with the sequences of the CV (Fig.7a) and CA (Fig.7c) results. Moreover, as shown in Fig.7a, the onset potentials of EOR on catalyst c_1, c_2 and c_3 were centered at about -0.68V. That is to say, prior to the EOR process, PdO of the studied catalysts has been totally electrochemically reduced to be metallic Pd, and then, the newly formed metallic Pd was used to electro-catalyze the EOR process. Also, it was well known that the peak area of a CV curve had a positive correlation with the amount of electric charge transferred in an electrochemical reaction. That is, the largest amount of metallic Pd was created on catalyst c_1 prior to the EOR process when using c_1 as the electrocatalyst to boost the EOR process. As a result, the largest peak current of CV as well as the largest polarized current density of CA was delivered by catalyst c_1. According to the previous work [64], the electrochemical surface areas (ECSA) of the Pd-based catalysts can also be approximately calculated using the CV curves of the studied Pd-based catalyst in 1 M KOH. To be more precise, the ECSA value of a Pd-based catalyst can be estimated using the following equation [64],

$$ECSA= Q_{PdO} /(m\times C\times \nu) \quad (1)$$

In equation (1), Q_{PdO} was the electric charge that was used to electrochemically reduce monolayer PdO, m was the mass of metallic Pd on the working electrode. C was 420 μC cm^{-2} [64], ν was 50 mV s^{-1}. Thus, only Q_{PdO} and m were two variables in above equation. Generally, in the CV test, the amount of electric charge transferred in an electrochemical reaction was directly proportional to its corresponding CV peak area [65].

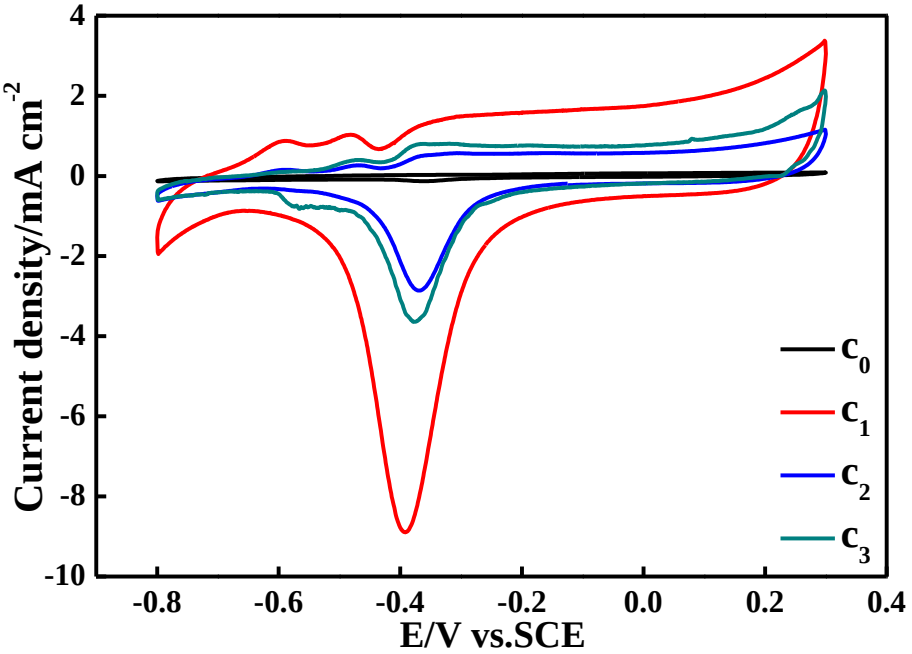

Figure 9. Cyclic voltammetry curves measured on various catalysts coated GC electrode in which the electrolyte was 1M KOH and the potential scanning speed was 50 mV s^{-1}. Curve c_0, c_1, c_2 and c_3 corresponded to the cases of using c_0, c_1, c_2 and c_3.

Thus, when supposing the m value was identical in all studied electrodes, catalyst c_1, due to its largest CV peak areas, should have the largest ECSA value among all studied catalysts. Further, being along with XPS analysis results, the exact ECSA values were calculated to be 29.89, 11.58 and 25.03 m^2 g_{Pd}^{-1} for catalyst c_1, c_2 and c_3, generating an increasing order of $c_2<c_3<c_1$ which accorded well with the CV (Fig.7a) and CA (Fig.7c) results.

(a)

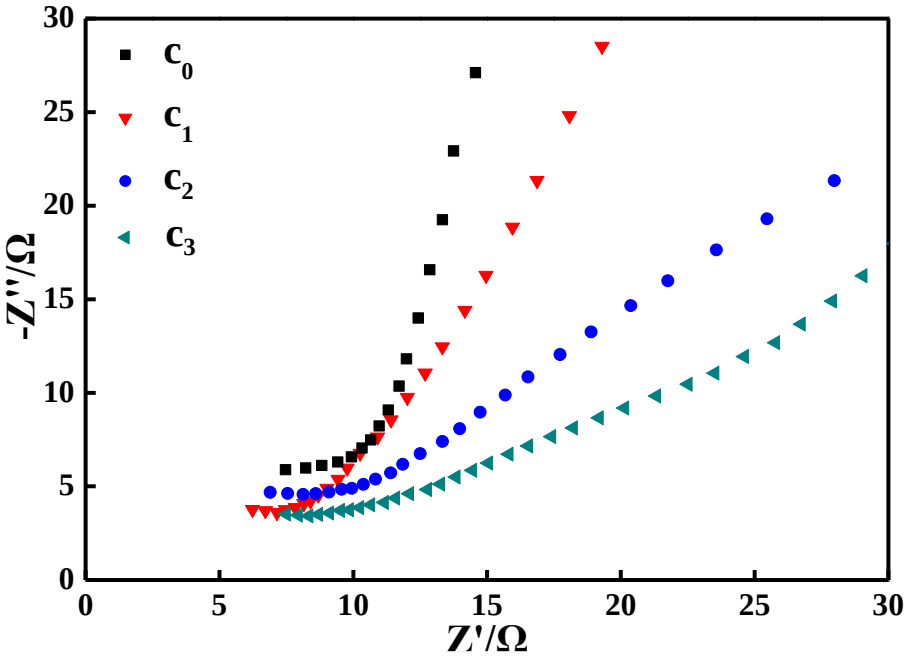

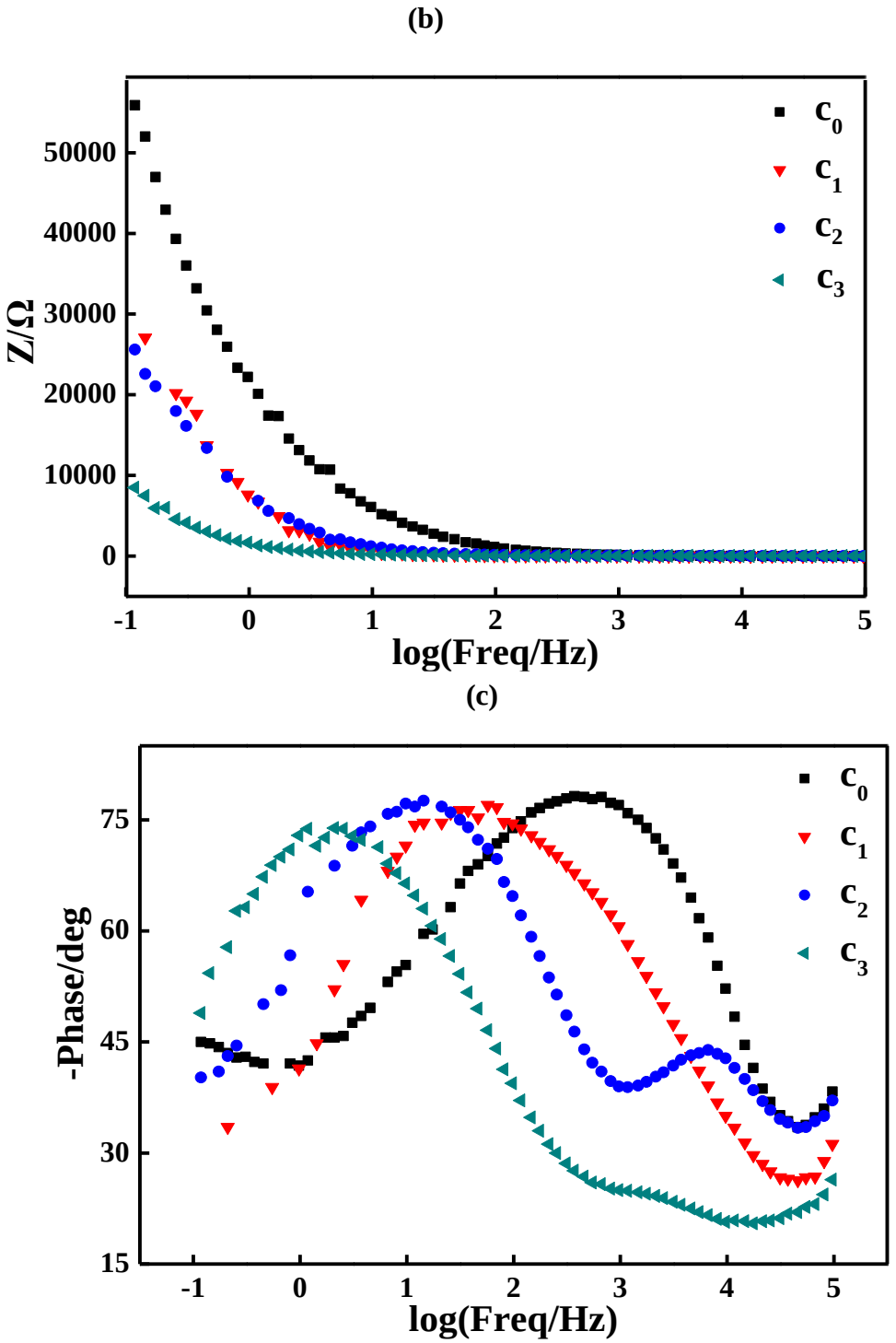

Figure 10. EIS measurements results for all studied catalysts which were carried out in the electrolyte solution containing 1M KOH and 1M ethanol. Curve c_0, c_1, c_2 and c_3 corresponded to the cases of using c_0, c_1, c_2 and c_3. **(a)** Nyquist plots measured on various catalysts coated GC electrode. **(b)** Curves describing the relationship between the total resistance and the frequency. **(c)** Bode plots measured on various catalysts coated GC electrode.

The Nyqusit plots, one typical curve of EIS plots, of all studied catalysts are illustrated in figure a of Fig.10. Generally speaking, the Nyquist curve of an electrochemical reaction was

constructed by a semicircle appearing in the higher frequency region and a 45° sloped line emerging in the lower frequency region [66]. And approximately, the charge transfer resistance value (R_{ct}) of an electrochemical reaction was equal to the diameter of the semicircle [67]. That is, the smaller semicircle commonly corresponded to a faster dynamic process. In figure a, for all studied catalysts, only a straight line was presented in the higher frequency region which strongly indicated that the R_{ct} values for EOR were too lower to be measured. The curves describing the relationship between the frequency and the total resistance are presented in figure b of Fig.10. Clearly, in the total frequency range, the total resistance value of catalyst c_0 was significantly higher that of other three catalysts, which substantially indicated that the introduction of NiO into the final catalysts was a feasible way to greatly reduce the total resistance values of the working electrodes. The Bode plots of all studied catalysts are presented in figure c of Fig.10. For catalyst c_0 and c_1, a huge symmetrical peak was presented in the whole frequency region. And the symmetrical peak centers for catalyst c_0 and c_1 were respectively positioned at about logf=2.7 and 1.5, respectively. In the case of catalyst c_2 and c_3, two symmetrical peaks were displayed in their own Bode plots. That is, the shape of Bode plot for c_0 and c_1 was rather different from that of the Bode plots for catalyst c_2 and c_3, suggesting that the microstructures of c_0 and c_1 was varied from that of c_2 and c_3, which was well in accordance with the SEM characterization results (Fig.6b).

To sum up, in this work, as compared to the Ni free Pd based catalyst (catalyst c_0), all Ni-containing Pd based catalysts prepared using Ni_2O_3 and $PdO{\cdot}H_2O$ as the starting materials exhibited a significantly promoted electrocatalytic activity towards EOR. The larger content of metallic Pd, the co-existence of huge spherical particles and sawdust-shaped particles, the larger ECSA value as well as the smaller value of R_{ct} were demonstrated to be the main reasons providing catalyst c_1 a significant electrocatalytic activity towards EOR. Also, in this work, besides Ni, Pd and O, no other elements as impurities were introduced in the whole preparation process of the final catalysts, which was thought to be the main novelty of this work compared to the previous works, being very meaningful for a practical long-life fuel cell. Preparing a Pd-Ni composite catalyst consisting of huge spherical particles and sawdust-shaped particles for EOR as well as showing its significant electrocatalytic activity towards EOR was considered as the main contribution of this preliminary work, which was very helpful to the progress of Pd-based EOR electrocatalysts.

4. CONCLUSIONS

In this work, firstly, a precursor containing NiO and carbon material was prepared through a hydrothermal process assisted air calcination method in which Ni_2O_3 and glucose were utilized as the reactants. And then, a Pd and Ni composite catalyst was fabricated via a hydrothermal method employing above as-prepared precursor and $PdO{\cdot}H_2O$ as the starting materials. All prepared samples were mainly characterized by XRD, SEM and XPS revealing that the added amount of Ni_2O_3 in preparing the precursors was a key factor which would directly influence the morphologies and the chemical components of the final catalysts. As indicated by the SEM images, huge spherical particles and sawdust-shaped particles were present in catalyst c_1, and only powder-shaped particles were

exhibited in catalyst c_2 and c_3. As analyzed by XRD and XPS, metallic Pd and NiO were the main substances of catalyst c_1, c_2 and c_3. More importantly, as indicated by CV and CA tests, as compared with catalyst c_0, catalyst c_1, c_2 and c_3 showed much better electrocatalytic activities towards EOR, indicating that the presence of NiO in the final catalysts was very beneficial to the electrocatalytic activity improvement of the pure Pd-based catalyst (catalyst c_0). Particularly, catalyst c_1, due to its higher content of metallic Pd, special morphology (co-existence of huge spherical particle and sawdust-shaped particles) and larger ECSA value, delivered the best electrocatalytic performance towards EOR. It should be emphasized that in the CA test, the polarized current density of EOR measured on c_1 was about as high as 2.68 mA cm^{-2} even after 7200 s, which strongly indicated that catalyst c_1 was a promising EOR electroocatalyst. Preparing a novel kind of precursor and showing the significant electrocatalytic activity of catalyst c_1 for EOR were the major dedications of this preliminary work, which, due to the lower preparation cost as well as the relatively pure system (besides O, Pd and Ni, no other elements were introduced into the final catalysts), was very favorable to the further exploration of the Pd and Ni composite EOR electrocatalysts.

ACKNOWLEDGEMENTS
This work was financially supported by Technical Innovation Advanced Research Foundation of Hebei Normal University (L2018K03) and Graduate student innovation ability training program of Hebei Normal University (CXZZSS2022060).

References

1. C. Laufkötter, J. Zscheischler and T. L. Frölicher, *Science*, 369 (2020) 1621.
2. M. S. Yeganeh, A. Jusufi, S. P. Deighton, M. S. Ide, M. Siskin, A. Jaishankar, C. Maldarelli, P. Bertolini, B. Natarajan, J. L. Vreeland, M. A. King and A. R. Konicek, *Sci. Adv.*, 8 (2022) eabm0144.
3. L. Cheng, X. Yue, L. Wang, D. Zhang, P. Zhang, J. Fan and Q. Xiang, *Adv. Mater.*, 33 (2021) 2105135.
4. J. J. Roy, S. Rarotra, V. Krikstolaityte, K. W. Zhuoran, Y. D.-I. Cindy, X. Y. Tan, M. Carboni, D. Meyer, Q. Yan and M. Srinivasan, *Adv. Mater.*, 33 (2021) 2103346.
5. R. G. Smead, *Clim. Energy*, 38 (2021) 23.
6. M. Li, H. Wang, W. Luo, P. C. Sherrell, J. Chen and J. Yang, *Adv. Mater.*, 32 (2020) 2001848.
7. J. Lin, J. Ding, H. Wang, X. Yang, X. Zheng, Z. Huang, W. Song, J. Ding, X. Han and W. Hu, *Adv. Mater.*, 34 (2022) e2200559.
8. Z. Guo, S. Zhao, J. Wang, Y. Wang, S. Zhai, T. Zhao and M. Ni, *Int. J. Energy Res.*, 46 (2021) 5997.
9. S. Zaman, L. Huang, A. I. Douka, H. Yang, B. You and B. Y. Xia, *Angew. Chem., Int. Ed.*, 60 (2021) 17832.
10. F. Xiao, Y.-C. Wang, Z.-P. Wu, G. Chen, F. Yang, S. Zhu, K. Siddharth, Z. Kong, A. Lu, J.-C. Li, C.-J. Zhong, Z.-Y. Zhou and M. Shao, *Adv. Mater.*, 33 (2021) 2006292.
11. Y. Wu, H. Zhou, A. Zhang and L. Zhao, *J. Power Sources*, 519 (2022) 230801.
12. Z. Feng, J. Huang, S. Jin, G. Wang and Y. Chen, *J. Power Sources*, 520 (2022) 230808.
13. P. Wang, H. Cui and C. Wang, *Nano Energy*, 66 (2019) 104196.
14. J. N. Tiwari, N. K. Dang, H. J. Park, S. Sultan, M. G. Kim, J. Haiyan, Z. Lee and K. S. Kim, *Nano Energy*, 78 (2020) 105166.

15. L. Zhang, Q. Chang, H. Chen and M. Shao, *Nano Energy*, 29 (2016) 198.
16. X. Wang, W. Fan, C. Zhang, M. Chi, A. Zhu, Q. Zhang and Q. Liu, *Electrochim. Acta*, 320 (2019) 134588.
17. A. M. M. Adam, M. Deng, A. Zhu, Q. Zhang and Q. Liu, *Electrochim. Acta*, 339 (2020) 135929.
18. X. Yu, J. Liu, J. Li, Z. Luo, Y. Zuo, C. Xing, J. Llorca, D. Nasiou, J. Arbiol, K. Pan, T. Kleinhanns, Y. Xie and A. Cabot, *Nano Energy*, 77 (2020) 105116.
19. H. Yang, H. Wang, H. Li, S. Ji, M. W. Davids and R. Wang, *J. Power Sources*, 260 (2014) 12.
20. Q. Yi and Q. Chen, *Electrochim. Acta*, 182 (2015) 96.
21. M. D. Obradović, Z. M. Stančić, U. Č. Lačnjevac, V. V. Radmilović, A. Gavrilović-Wohlmuther, V. R. Radmilović and S. Lj. Gojković, *Appl. Catal., B*, 189 (2016) 110.
22. A. Eshghi, E. S. Behbahani, M. Kheirmand and M. Ghaedi, *Int. J. Hydrogen Energy*, 44 (2019) 28194.
23. P.-F. Yin, M. Zhou, J. Chen, C. Tan, G. Liu, Q. Ma, Q. Yun, X. Zhang, H. Cheng, Q. Lu, B. Chen, Y. Chen, Z. Zhang, J. Huang, D. Hu, J. Wang, Q. Liu, Z. Luo, Z. Liu, Y. Ge, X.-J. Wu, X.-W. Du and H. Zhang, *Adv. Mater.*, 32 (2020) 2000482.
24. H. Wang, S. Jiao, S. Liu, H. Zhang, Y. Xu, X. Li, Z. Wang and L. Wang, *Chem.-Eur. J.*, 27 (2021) 14472.
25. D. Martín-Yerga, G. Henriksson and A. Cornell, *Int. J. Hydrogen Energy*, 46 (2021) 1615.
26. M. T. X. Nguyen, M.-K. Nguyen, P. T. T. Pham, H. K. P. Huynh, H. H. Pham, C. C. Vo and S. T. Nguyen, *J. Electroanal. Chem.*, 888 (2021) 115180.
27. Y. Shen, S. Lu, W. Xu, A. Lv, Z. Wang, H. Wang, G. Liu and Y. Zhang, *Electrocatalysis*, 11 (2020) 522.
28. S. Gomroki, Z. Yavari, A. R. Abbasian and M. Noroozifar, *Int. J. Appl. Ceram. Technol.*, 18 (2021) 2099.
29. X. Wu, X. Li, Y. Yan, S. Luo, J. Huang, J. Li, D. Yang and H. Zhang, *Front. Chem.*, 9 (2021) 683450.
30. K. Ding, Y. Wang, H. Yang, C. Zheng, Y. Cao, H. Wei, Y. Wang and Z. Guo, *Electrochim. Acta*, 100 (2013) 147.
31. Y.-Z. Zheng and M.-L. Zhang, *Mater. Lett.*, 61 (2007) 3967.
32. G. A. Gohar, T. Manzoor, A. Ahmad, H. Raza, A. Farooq, I. Karim, W. Iftikhar, M. Umar and F. Asad, *J. Alloys Compd.*, 817 (2020) 153281.
33. X. Sun and Y. Li, *Angew. Chem., Int. Ed.*, 43 (2004) 597.
34. T. Kumari, R. Gopal, A. Goyal and J. Joshi, *J. Inorg. Organomet. Polym. Mater.*, 29 (2019) 316.
35. C. Sandt, J. Waeytens, A. Deniset-Besseau, C. Nielsen-Leroux and A. Réjasse, *Spectrochim. Acta, Part A*, 258 (2021) 119841.
36. J. Wu, C. Jin, Z. Yang, J. Tian and R. Yang, *Carbon*, 82 (2015) 562.
37. P. Boomi, R. Ganesan, G. P. Poorani, S. Jegatheeswaran, C. Balakumar, H. G. Prabu, K. Anand, N. M. Prabhu, J. Jeyakanthan and M. Saravanan, *Int. J. Nanomed.*, 15 (2020) 7553.
38. F. Davar, Z. Fereshteh and M. Salavati-Niasari, *J. Alloys Compd.*, 476 (2009) 797.
39. B. S. Rathore, N. P. S. Chauhan, S. Jadoun, S. C. Ameta and R. Ameta, *J. Mol. Struct.*, 1242 (2021) 130750.
40. N. Afify, *Mater. Sci. Eng., B*, 273 (2021) 115399.
41. V. Biju and M. Abdul Khadar, *Spectrochim. Acta, Part A*, 59 (2003) 121.
42. V. Pogorelov, I. Doroshenko, P. Uvdal, V. Balevicius and V. Sablinskas, *Mol Phys*, 108 (2010) 2165.
43. K. Yamamoto, *Vacuum*, 84 (2010) 638.
44. Z. Huang, L. Shi, Y. Muhammad and L. Li, *J. Colloid Interface Sci.*, 586 (2021) 423.
45. S. Thareja and A. Kumar, *J. Phys. Chem. C*, 125 (2021) 24837.
46. Y. Park, N. H. Kim, S. B. Cho, J. M. Kim, G. C. Kim, M. S. Kim, S. M. Lee, I.-Y. Eom, H. C. Choi and Y. M. Jung, *J. Mol. Struct.*, 974 (2010) 139.

47. J. Li, D. Yan, S. Hou, T. Lu, Y. Yao, D. H. C. Chua and L. Pan, *Chem. Eng. J.*, 335 (2018) 579.
48. A. Molak and M. Pilch, *J. Appl. Phys.*, 119 (2016) 204901.
49. J. Chen, G. Feng, F. Jiang, L. Yin, Q. Zhao, S. Lan, X. Zhang, J. Liu, Q. Hu and W. Jiang, *Ceram. Int.*, 47 (2021) 33242.
50. T. S. Almeida, Y. Yu, A. R. de Andrade and H. D. Abruña, *Electrochim. Acta*, 295 (2019) 751.
51. M. T. X. Nguyen, M.-K. Nguyen, P. T. T. Pham, H. K. P. Huynh, H. H. Pham, C. C. Vo and S. T. Nguyen, *J. Electroanal. Chem.*, 888 (2021) 115180.
52. H. Zhang, Y. Liu and X. Zhang, *Chin. J. Catal.*, 32 (2011) 1693.
53. D. Chen, R.-H. Zhang, Q. Y. Hu, Y.-F. Guo, S.-N. Chen, X.-W. Zhou and Z.-X. Dai, *J. Electroanal. Chem.*, 834 (2019) 241.
54. H. Jahromi, S. Adhikari, P. Roy, E. Hassani, C. Pope, T. S. Oh and Y. Karki, *Fuel Process. Technol.*, 215 (2021) 106737.
55. A. Roy and D. Das, *J. Phys. Chem. Solids*, 160 (2022) 110307.
56. M. Kaur, R. A. Mir, I. Chauhan, K. Singh, U. Krishnan, M. Kumar, P. Devi, O. P. Pandey and A. Kumar, *Appl. Surf. Sci.*, 559 (2021) 149982.
57. K. Ding, H. Gu, C. Zheng, L. Liu, L. Liu, X. Yan and Z. Guo, *Electrochim. Acta*, 146 (2014) 585.
58. W. Zhu, D. Liu, J. Trottier, C. Gagnon, J. Howe, A. Mauger, C. M. Julien and K. Zaghi, *J. Power Sources*, 298 (2015) 341.
59. K. G. Mikheev, A. S. Saushin, R. G. Zonov, A. G. Nasibulin and G. M. Mikheev, *J. Nanophotonics*, 10 (2016) 012505.
60. M. Kurnatowska, L. Kepinski and W. Mista, *Appl. Catal., B*, 117-118 (2012) 135.
61. Z. X. Liang, T. S. Zhao, J. B. Xu and L. D. Zhu, *Electrochim. Acta*, 54 (2009) 2203.
62. K. Ding, C. Li, Y. Zhang, L. Wang, B. Wei, X. Shi and X. He, *Int. J. Hydrogen Energy*, 43 (2018) 1523.
63. E. Leal da Silva, A. Cuña, C. R. Plascencia, C. Radtke, N. Tancredi and C. de Fraga Malfatti, *Clean Technol. Environ. Policy*, 22 (2020) 259.
64. Z. Cui, J. Hu, X. Jiang, D. Zhang and C. Fang, *J. Alloys Compd.*, 855 (2021) 157385.
65. K. Ding, Z. Jia, Q. Wang, X. He, N. Tian, R. Tong and X. Wang, *J. Electroanal. Chem.*, 513 (2001) 67.
66. K. Ding, L. Liu, Y. Cao, X. Yan, H. Wei and Z. Guo, *Int. J. Hydrogen Energy*, 39 (2014) 7326.
67. K. Ding, G. Yang, S. Wei, P. Mavinakuli and Z. Guo, *Ind. Eng. Chem. Res.*, 49 (2010) 11415.